Journal of Applied Fluid Mechanics, Vol. 18, No. 12, pp. 3101-3115, 2025.
Available online at www.jafmonline.net, ISSN 1735-3572, EISSN 1735-3645.
https://doi.org/10.47176/jafm.18.12.3593

Centrifugal Compressor Instability and the Reverse Propagation Mechanism in Diffusers

Y. Ping[1,2], M. Wang[3†], X. Zhang[1,2], K. Bai[1,2], F. Qu[3], Z. Tao[1,2] and C. Wang[3]

[1] *State Key Laboratory of Clean and Efficient Turbomachinery Power Equipment, Deyang 618000, China*
[2] *Dongfang Electric Corporation Dongfang Turbine Co., LTD, Deyang 618000, China*
[3] *Harbin Engineering University, College of Power and Thermal Energy, Harbin, 150001, China*

†*Corresponding Author Email: wangmeng_a@hrbeu.edu.cn*

ABSTRACT

At low flow rates, centrifugal compressors often experience aerodynamic instabilities, posing a crucial concern for gas turbine engineers. This study focused on a standard centrifugal compressor and investigated its aerodynamic behavior through numerical simulations in both steady and unsteady full-annulus states. Additionally, it analyzed diffuser stability by evaluating the signals associated with rotating stall. Results indicated that, as the flow rate decreases and the flow shifts downstream in the full-cycle model, the non-uniformity of the Mach number in the circumferential direction near the blockage region increases from 8.13% to 25.52%. Under the design condition, the circumferential non-uniformity rises from 15.18% to 24.12%. When the compressor becomes unstable, the centrifugal impeller exhibits rotational instabilities with a disturbance frequency of 1304.61 Hz, corresponding to 23.95% of the blade passing frequency. The conclusions of this study provide fresh insights into unsteady flow characteristics in centrifugal compressors and offer practical guidelines for enhancing the operational stability of microturbine units.

Article History

Received April 10, 2025
Revised July 2, 2025
Accepted July 27, 2025
Available online October 6, 2025

Keywords:

Centrifugal compressor
Unsteady flow
Diffuser
Stall
Circumferential non-uniformity

1. INTRODUCTION

With the rapid advancement of science and technology, alongside the increasing demand for industrial production, concerns about energy, the environment, and climate change are becoming central issues for major global powers. In response to these challenges, microturbines have emerged as a promising technology with significant growth potential (Yoon & Song 2014). The centrifugal compressor plays a critical role in the microturbine system. Its aerodynamic performance directly influences the overall operational efficiency of microturbines, making it a key factor in their effective functioning (Fujisawa et al., 2014).

The unstable flow phenomena that occur at low flow rates—such as stall, surge, and rotational instability—are the primary factors limiting the operational flow range of compressors (Day, 2016). In centrifugal compressors with vaneless diffusers, surge often arises in both the impeller and diffuser regions. Sheng-ling & Zheng-xian (2019) investigated the stall behavior in isolated centrifugal impellers and compared it with that in axial compressors, highlighting that unstable flow within the compressor results from interactions between leading-edge vortices, channel vortices, and low-speed secondary vortices in centrifugal impellers. Through experimental measurements, Zhang, H. et al. (2022) conducted an in-depth study of stall induced by rotational instability in isolated impellers. This study reported that, as the flow rate decreases, a vortex structure is formed on one side of the casing, which leads to a rotational instability at a specific circumferential position within the compressor. This instability gradually spreads across the entire circumference, causing inlet blockage in the impeller and ultimately leading to stall.

Zhang (2020) and Zhang et al. (2020) investigated the stall modes of wide-blade-less diffusers with different radius ratios. In wide bladeless diffusers, stall occurs due to a continuous upstream from the outlet. Zhang (2021) and Zhang et al. (2021) analyzed the initiation of rotating stall in wide and narrow bladeless diffusers, finding that narrow diffusers experience localized recirculation and inward expansion, whereas wide diffusers experience core flow distortion. According to Zheng (2019), wide and narrow bladeless diffusers can be differentiated on the basis of aspect ratio, with the dividing threshold lying between 0.093 and 0.13. This suggests that, while the

mechanisms leading to stall formation differ between wide and narrow diffusers, the characteristics of the resulting stall clusters remain similar. Using a full-perimeter modeling approach, Marconcini et al. (2016) illustrated the gradual formation of three stall clusters in a bladeless diffuser, with perturbation frequencies of the stall clusters measuring 4.5 times the rotational frequency of the impeller.

The stall behavior in a lobed diffuser is more complex. Zhang et al. (2022b) analyzed stall in a high-pressure-ratio centrifugal compressor with a lobed diffuser using full-loop numerical simulation. The stall mass propagates downstream in the diffuser when influenced solely by the angle of attack. However, when stall clusters are affected by several factors—namely excitation, angle of attack, and the number of stall clusters— reverse propagation in the direction of impeller rotation is observed. Hu et al. (2021) determined the cause of stall by making overall and local adjustments to the installation angle of diffuser blades. Hu found that the flow stability of the diffuser deteriorates when the diffuser blades rotate to a negative angle. Xue & Wang (2020) discovered that, in vaneless diffusers and vaned diffusers with the installation angle deviates from the design specifications, backflow first occurs in the low-pressure area on the casing side, forming modal stall. In vaned diffusers with a design installation angle, a tip stall forms in the high-pressure area.

In summary, extensive research has been conducted on unsteady flow in centrifugal compressors, primarily using three approaches: theoretical modeling, numerical simulation, and experimental measurement (Emmons et al., 1955). These studies have established a solid theoretical foundation. However, most research on rotational instability has focused on axial flow compressors and vane grid tests, with relatively limited literature addressing centrifugal compressors (Greitzer & Moore 1986, McDougall et al. 1990; Day, I. J. 1993). To better understand the variation in stability parameters within compression systems and the propagation mechanisms of diffuser stall clusters, this study examined the flow characteristics of and peripheral instability mechanisms in centrifugal compressors. This analysis used both single-pass and full-periphery numerical simulations, considering the complexity of centrifugal compressor structures, the variability of stall phenomena across different compressors, and the lack of correlation between instability modes.

In recent years, extensive research has been conducted on the unstable flow mechanism in centrifugal compressors with diffusers. Zhenzhong conducted experimental studies on flow instability in centrifugal compressors with blade diffusers and meticulously expounded and analyzed the causes and mechanisms of instability across the operating range. According to this study, the compressor experiences different flow instability patterns depending on the operating conditions. (Sun et al. 2018). However, the flow evolution process remains unclear. Lianchao was the first to conduct a non-steady full-loop simulation of centrifugal compressors. The study showed that flow instability primarily occurs in the impeller part of the compressor. (Xu et al. 2023). However, it neglects the interaction between the impeller and diffuser. To examine the influence of diffuser–impeller interactions on unstable flow processes, we conducted a full-loop non-steady study and analyzed the unstable flow mechanism using temporal and spatial evolutions of flow.

Table 1 Geometric parameters of the centrifugal compressor used in the study

Geometric parameter	Value
Number of main blades	15+15
Wedge diffuser	24
Design speed (rpm)	21789
Impeller outlet tangential velocity (m/s)	492
Inlet leaf top radius (mm)	210
Exit radius (mm)	431
Inlet blade height (mm)	64
Outlet blade height (mm)	17
Inlet Leaf Top Clearance (mm)	0.1524
Outlet lobe top clearance (mm)	0.2030

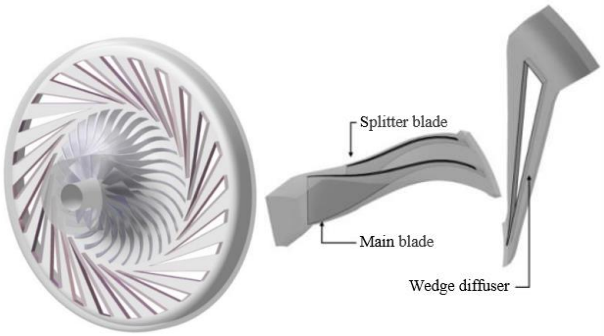

Fig. 1 Full and single-channel models of the centrifugal compressor used in the study

2. NUMERICAL METHOD SETUP AND VALIDATION

This study used a sophisticated high-pressure-ratio single-stage centrifugal compressor (Mckain & Holbrook 1997) with a design flow rate of 1.66–4.54 kg/s. The model of the centrifugal compressor is displayed in Fig. 1, and its principal geometric characteristics are listed in Table 1.

2.1 Numerical Boundary Condition

In this paper, CFX is used for numerical simulation. Both steady-state and unsteady-state calculation methods were employed in the full-annulus simulation software. The steady-state calculation model was defined as follows: the total temperature at the compressor inlet was set as 288.15 K, with a total pressure of 101,325 Pa as the boundary condition. The outflow was modeled using an average hydrostatic pressure outlet, and the pressure distribution was determined using the radial equilibrium equation. For the unsteady-state calculation, a transient rotor–stator interface was used, whereas the compressor outlet was modeled using the standard throttle valve mathematical model (Wang, 2020), as shown in Eq. (1). Adiabatic and non-slip conditions were applied to the wall

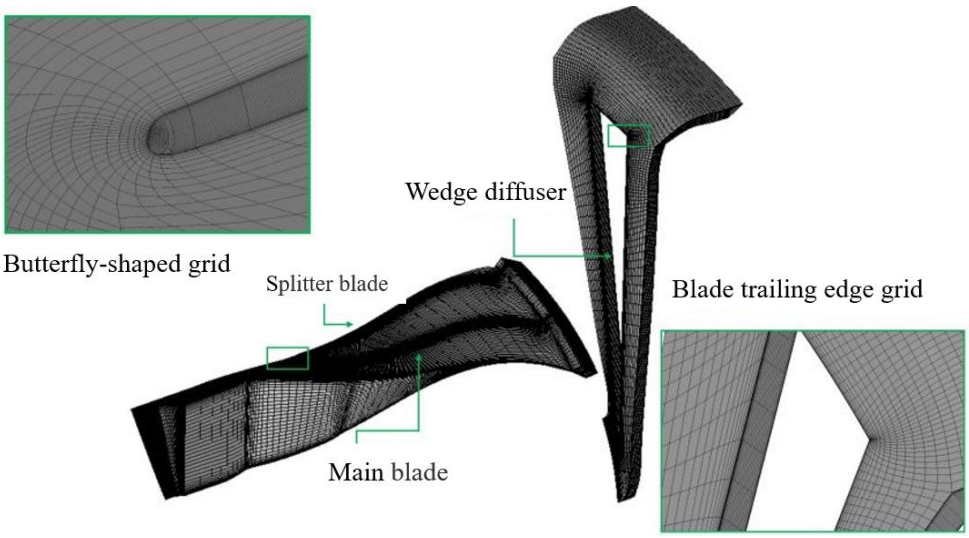

Fig. 2 Mesh for single-channel

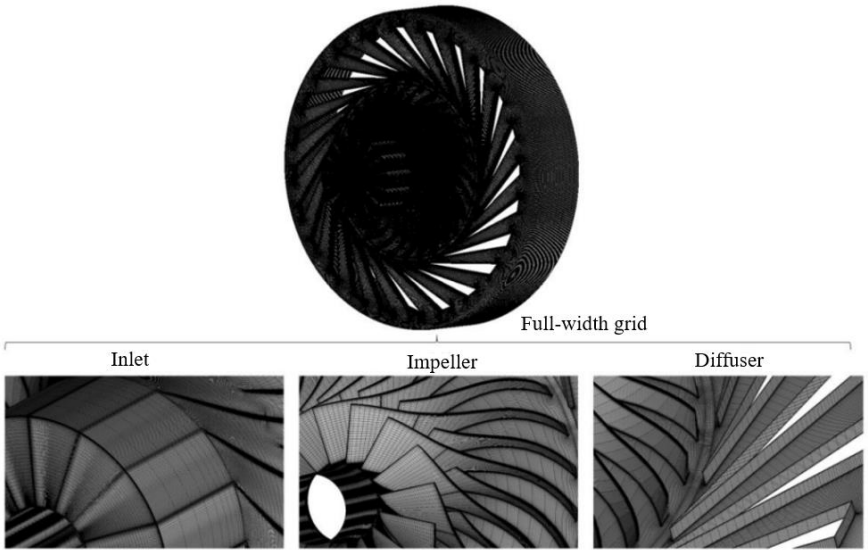

Fig. 3 Mesh for full-channel centrifugal compressor

surfaces of components such as the impeller, diffuser, casing, and hub.

$$P_{out} + P_{ref} + km_{out}^2(t), \quad (1)$$

where P_{out} denotes the instantaneous pressure (Pa) at the outlet of the pressurizer; P_{ref} is the set reference pressure (Pa); k is the throttling coefficient; m_{out} (t) denotes the instantaneous mass flow rate at the outlet of the pressurizer in kg/s.

A second-order upwind format was used for the numerical discretization scheme, whereas the second-order backward Euler method was employed for time discretization. For turbulence modeling, a first-order difference was applied. The convergence criterion was set to 10^{-6} for the full-periphery unsteady-state calculations (Spakovszky, 2004).

To ensure the grid quality of the impeller, an appropriate topology was adopted for the impeller, diffuser, and extension section. The number of generated single-channel grids were 0.483, 0.643, 0.82, 1.01, and 1.171 million, which were designated as mesh-1, mesh-2, mesh-3, mesh-4, and mesh-5, respectively. A structured grid was adopted, and the height of the first layer of the grid satisfied the requirement that y+ is within the range of (1, 10). Figure 4 compares the compressor performance at three typical operating conditions at 100 % design speed. As the number of grids increases, the aerodynamic performance of the compressor gradually declines, and the mesh-4 grid scheme satisfies the requirements for subsequent calculations. The single-channel grid distribution is shown in Fig. 2. The full-periphery mesh was generated by rotating the single-channel grid according to its periodicity, resulting in a total of 17.404 million grid cells. Figure 3 shows the peripheral grid distribution, which consists of 17.404 million rotating peripheral cells, out of which 11.446 million correspond to the impeller components and 5.958 million represent the wedge diffuser cells. Finally, the total number of

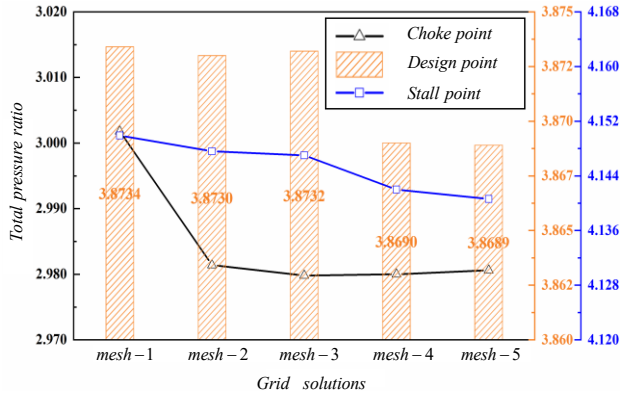

(a) Total pressure ratio for different numbers of grids

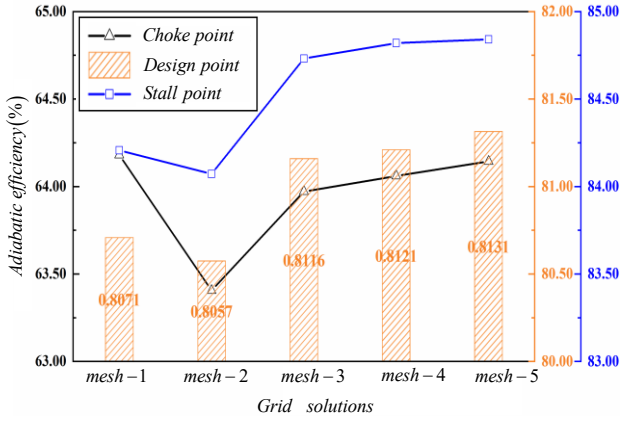

(b) Adiabatic efficiency for different numbers of grids

Fig. 4 Comparison of mesh independence verification

single-channel grids was determined to be 1.011 million. A total of 17.404 million grids were used in the study.

2.2 Validation of Numerical Methods

The Spalart–Allmaras single equation model was used as the turbulence model, and an enhanced wall function was activated. Our rationale for selecting the Spalart–Allmaras model was based on a study by Ge et al. (2023). A previous study compared the numerical results from three different models for a pipe diffuser (Han, 2014). The results predicted by the Spalart–Allmaras, k-ε, and SST models did not considerably differ from the actual results. Additionally, the Spalart–Allmaras model has been used to investigate tip leakage flow and instability in centrifugal compressors. The one-equation Spalart–Allmaras model is extensively used for evaluating turbulence closure as it can accurately calculate viscous boundary-layer turbulent flow and small- or medium-scale separated flow characteristics. The high-precision solution mode was used for the numerical difference scheme and the solution accuracy of the turbulence model. For the Spalart–Allmaras model, the first layer of the grid should satisfy the condition that y+ is within the range of (1, 10). In this study, the height of the first layer of the grid satisfied the y+ requirement.

In 1997, Skoch et al. (1997) assessed the characteristics of a DDA404-III centrifugal compressor at all operating conditions and the internal flow field of the LDV. The numerical simulation results were compared with the measurement results. Figure 5 compares the results of the full-channel simulation, single-channel numerical simulation, and experimental measurement of the characteristic line results at 100% rpm.

As shown in Fig 5, at 100% rotational speed, the numerical results closely align with the experimental data. Both single-channel and full-annulus simulation results display analogous trends but exhibit differences under certain conditions. In high-flow near-choking and near-surge conditions, full-annulus simulation results are closer to the experimental results. This can be attributed to its efficient management of the intense circumferential distortions from the shock zones at the diffuser inlet. Nevertheless, compared to single-channel simulation, the full-annulus characteristic line does not fully correlate with the experimental data in some mid-flow cases. Full-annulus simulation includes both steady and unsteady methods. At high flow rates, the non-oscillatory flow enables steady full-annulus simulation to capture flow states. However, as backpressure increases and the compressor experiences surge with flow disturbances and parameter fluctuations, steady-state simulation fails to

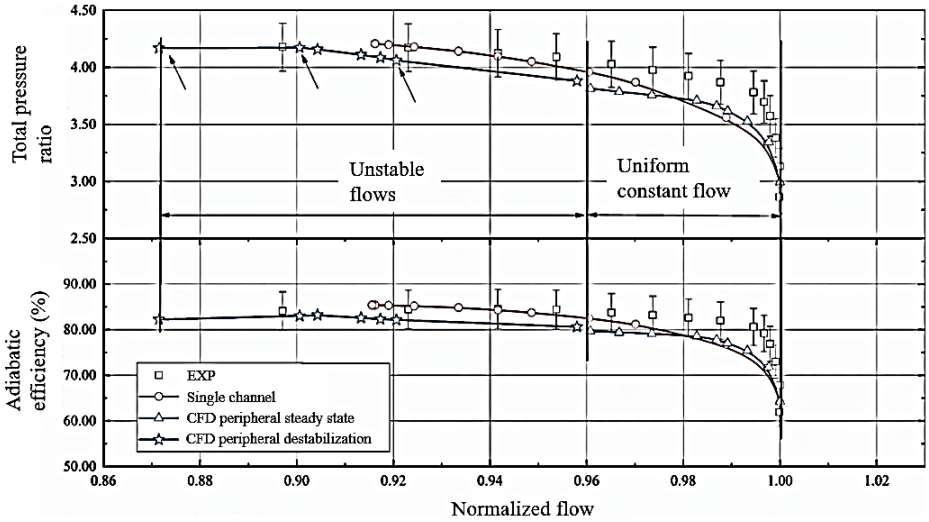

Fig. 5 Verification of full-channel numerical simulation

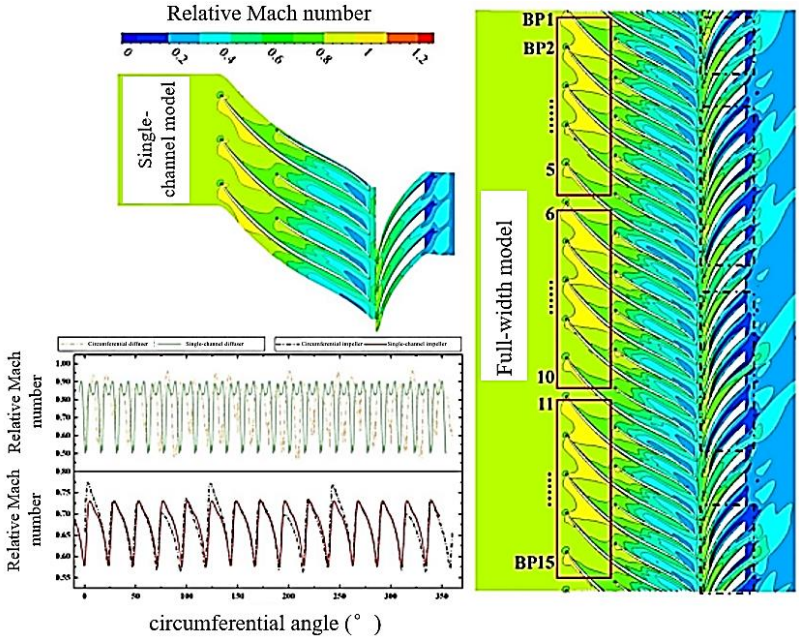

Fig. 6 Mach number for full- and single-channel models at design point

converge, necessitating the switch to unsteady methods. As shown in Fig. 5, when using an unsteady simulation, errors in compressor-performance prediction increase slightly. The full-annulus numerical method outperform the single-channel model in predicting near-surge conditions, with simulation errors within 5%, fulfilling research requirements.

3. ANALYSIS OF RESULTS

3.1 Characterization of Steady-State Flow in the Centrifugal Compressor

The steady state computation primarily focusses on the flow distribution structure of the pressurizer along the entire perimeter space. The excitation structure at the leading edge of the impeller markedly differs between the full-perimeter and single-channel models. As illustrated in Fig. 6, as the flow rate decreases, the positive angle of attack between the incoming flow and blade increases. In the full-perimeter model, the negative angle of attack at the leading edge increases at locations BP1, BP2, and BP3. The intensity of the excitations is higher on the pressure surface, whereas the suction-surface excitations are concentrated at the front end of the channel. This leads to a specific blocking effect on the incoming flow, causing the blocking zone in the channel to disappear. Additionally, pressure-surface excitations are reduced, and the negative angle of attack decreases at BP4 and BP5.

Moreover, a substantial degree of circumferential non-uniformity is observed in the diffuser, as indicated by the distribution of the Mach number. In the single-channel diffuser model, no flow separation occurs at 95% of the lobe height. However, in the full-perimeter calculation, suction-side separation affects 45.8% of the diffuser channels, whereas pressure-side separation impacts only 12.5% of the diffuser channels.

As shown in Fig. 7, static pressure exhibits a sinusoidal distribution around the perimeter in the single-channel diffuser model. In addition, three pressure spikes are observed at the leading edge of the diffuser, along with a distinct pressure fluctuation curve at the diffuser trailing edge.

The Mach number and pressure distributions at the leading edges of the diffuser and impeller for both the single-pass and full-perimeter models are presented in Fig. 8 using boxplots. The statistics for the circumferential parameters at the diffuser leading edge indicate that the non-uniformity in pressure worsens with decreasing flow rate, whereas the non-uniformity in the Mach number remains relatively unchanged. In the full-perimeter model, both the circumferential non-uniformity of the Mach number and static pressure at the impeller leading edge increase as the flow rate decreases, with greater variability observed in the upper and lower peaks of the boxplots.

This increase in variability is attributed to the fact that the aberrations at the impeller leading edge are not the sole contributor to the circumferential variation in Mach number at the diffuser leading edge near the blockage point; the blockage at the diffuser throat further exacerbates the non-uniform distribution characteristics of the Mach number. Additionally, disturbances caused by the blades naturally introduce non-uniformity in the circumferential distribution of parameters at both the diffuser and impeller leading edges. Further quantitative analysis was conducted to assess the non-uniformity of incoming-flow parameters at the leading edges. The formulas for calculating the maximum non-uniformity in the Mach number and pressure of the incoming flow are provided below.

$$\delta_{Ma} = \frac{\left|Ma_{max} - Ma_{ave}\right|}{Ma_{ave}} \times 100\% \tag{2}$$

$$\delta_{P} = \frac{\left|P_{max} - P_{ave}\right|}{P_{ave}} \times 100\% \tag{3}$$

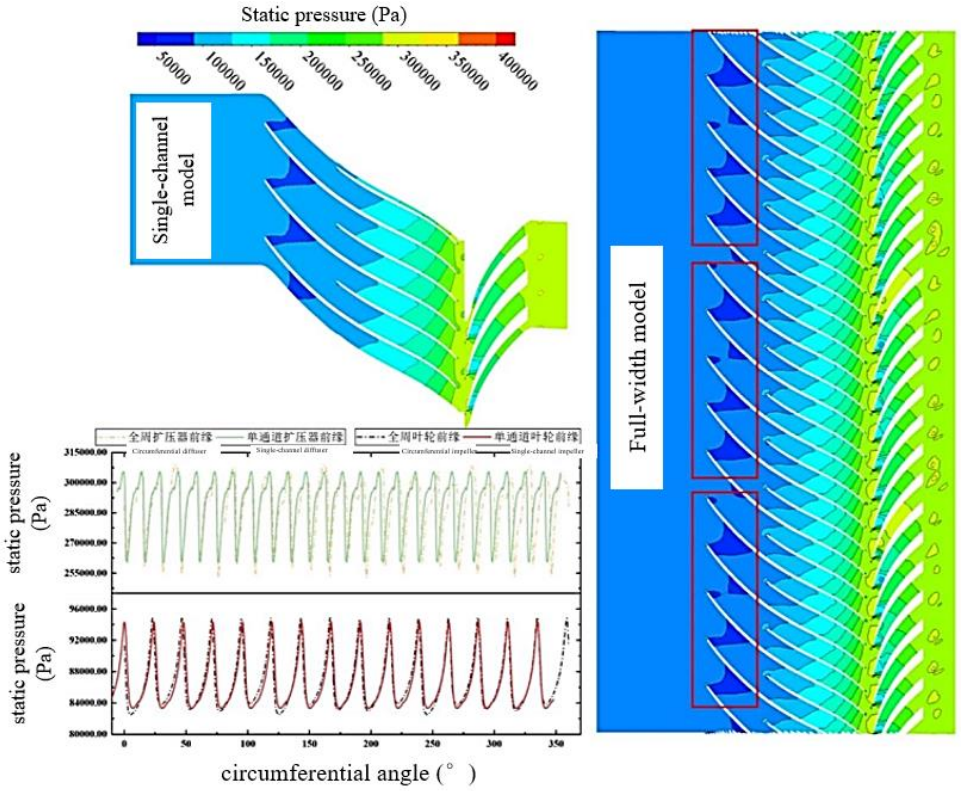

Fig. 7 Pressure for full- and single-channel models at design point

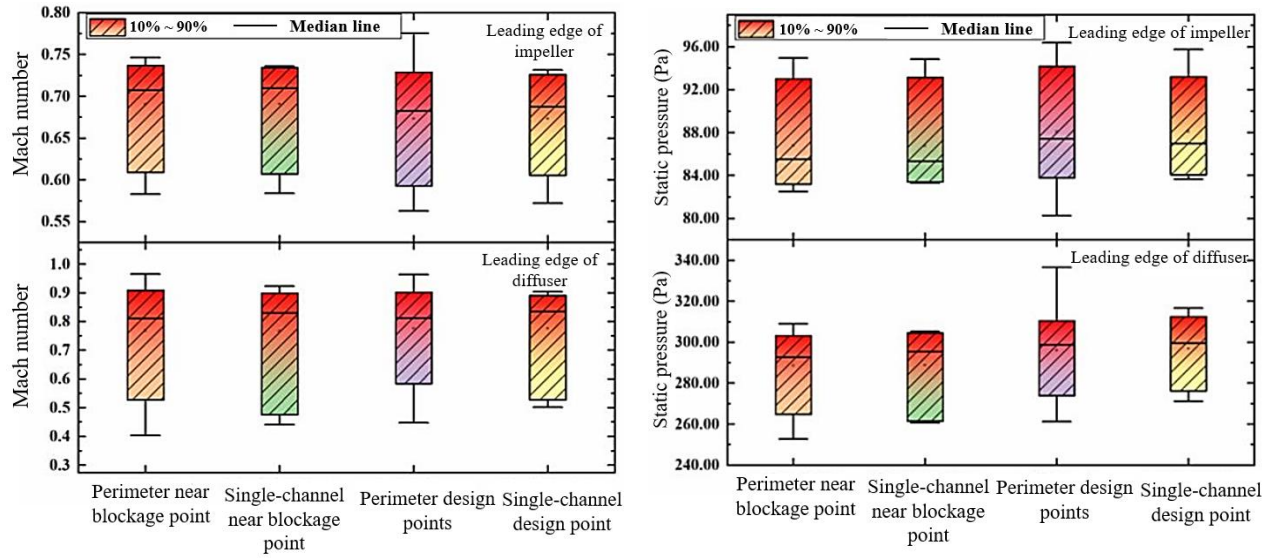

(a) Full channel models (b) Single channel models

Fig. 8 Boxplots of circumferential parameters for full- and single-channel models

In summary, the circumferential characteristics of the incoming flow become increasingly non-uniform at the impeller leading edge and continues downstream along the impeller channel, leading to increased circumferential distortions at the diffuser leading edge. As the compressor flow rate gradually decreases, the diffuser leading edge exhibits pronounced non-uniform flow characteristics. Additionally, significant reflux occurs on the suction surface of certain diffuser blades, further exacerbating the circumferential non-uniformity at the diffuser leading edge.

As shown in Fig 9, the maximum non-uniformities in Mach number and pressure are higher for the full annular model than for the single-channel model. In the full annular model, the circumferential non-uniformity of the Mach number at the blockage point increases from 8.13% at the leading edge of the impeller to 25.52% at the leading edge of the diffuser. At the design point, the maximum non-uniformity of the Mach number rises from 15.18% to 24.12%. The circumferential maximum non-uniformity of pressure increases from 4.96% at the blockage point to 7.05% and from 8.90% at the design point to 13.73%. As

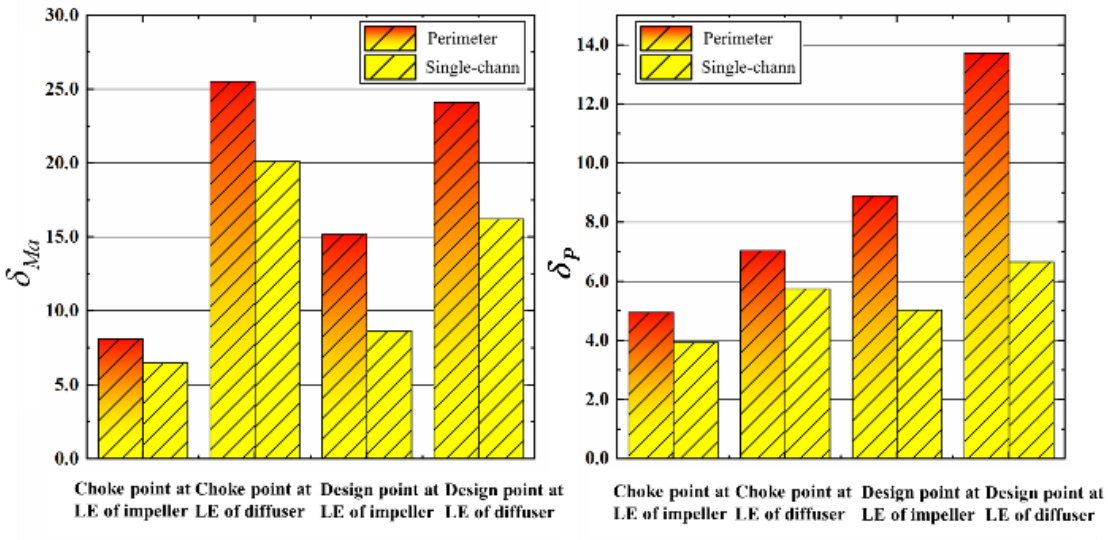

Fig. 9 Maximum non-uniformity distribution of incoming flow parameters

the flow rate decreases, the circumferential non-uniformity of the Mach number and pressure at the leading edge of the impeller increases. Additionally, the maximum non-uniformity of pressure at the leading edge of the diffuser rises, whereas the maximum non-uniformity of the Mach number slightly decreases. This indicates that, when the centrifugal compressor is close to the blockage state, the blockage at the throat of the diffuser considerably influences the Mach number for the upstream incoming flow. In summary, the circumferential non-uniformity of the incoming flow parameters originates at the leading edge of the impeller and propagates downstream through the impeller channel, thereby intensifying the distortion at the leading edge of the diffuser. Moreover, a decrease in flow rate increases the circumferential distortion at the leading edge of the impeller. The combined effect of these factors leads to strong unsteady flow and recirculation at the leading edge of the diffuser, further enhancing the circumferential non-uniformity.

3.2 Instability Mechanism of the Centrifugal Compressor

The flow state and dynamic pressure signals at critical locations within the centrifugal compressor were analyzed under three different flow coefficients: 0.0412, 0.0405, and 0.0390. A total of thirty pressure probes were deployed, with an acquisition frequency six times that of the blade passing frequency (BPF), enabling real-time detection of the internal flow and pressurized flow signals within the centrifugal compressor. The analysis focused on three flow directions at specific cross-sections: the leading edge of the main impeller, the leading edge of the diverter blade, and the leading edge of the diffuser at 95% leaf height. Figure 10 illustrates the distribution of the various pressure probes.

3.3 Analysis of Rotational Instability in Centrifugal Impeller

(1) Spatiotemporal characterization of pressure signals from centrifugal impeller

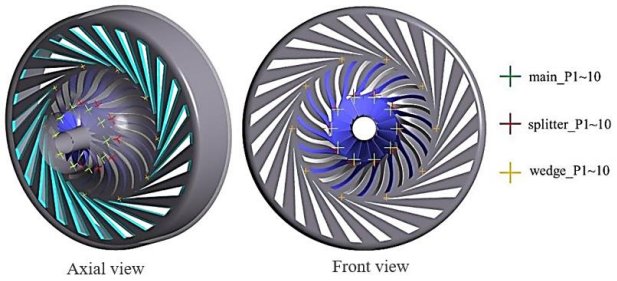

Fig. 10 Schematic of pressure-probe locations

Ten pressure signals from the leading edge of the impeller were studied in both time and space domains. The horizontal coordinate represented the time dimension as the number of rotor revolutions, the vertical coordinate represented the spatial dimension expanded to the circumferential angle, and the color represented the dimensionless value of the pressure signals at a given point at a given time.

On the leading edge of the impeller, seven discontinuous low-pressure strips and four high-pressure strips are observed when the flow coefficient φ is 0.0412, as shown in Fig. 11. The pressure signal distribution along the circumferential direction is not consistent with the results of the full circumferential steady state calculations, suggesting the existence of spatial periodicity. It demonstrates the prolonged persistence of circumferential inhomogeneity in the leading edge of the impeller, which continuously increases as the flow rate decreases. However, the disturbance frequency remains comparable to the passing frequencies of the blades, and the propagation path of pressure wave has not yet been formed in space. The results are comparable to the average results of the steady state calculation. At this time, it may be assumed that the circumferential distortion at the leading edge of the impeller is not sufficiently strong. Moreover, the pressure fluctuations cannot form a pressure propagation trajectory over the course of the entire week

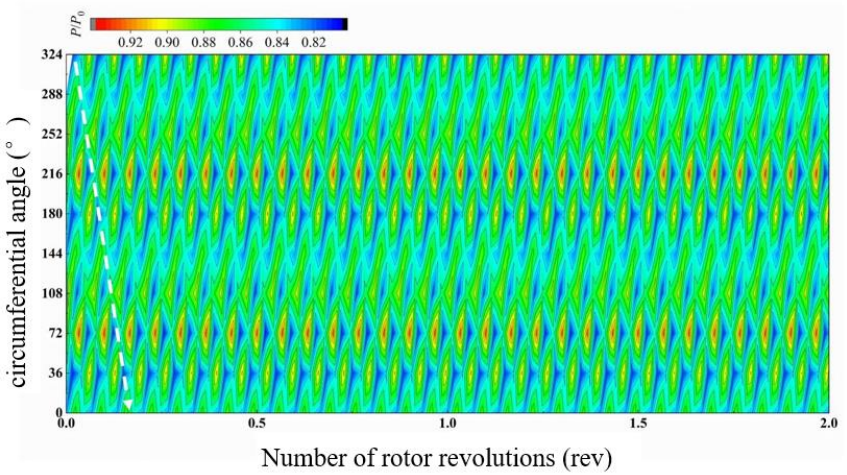

Fig. 11 Space–time diagram of the pressure signal at the leading edge of the impeller at φ = 0.0412

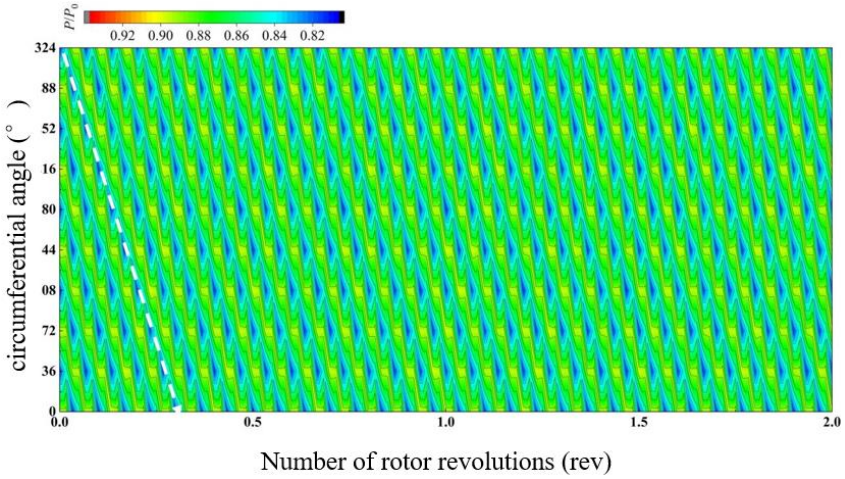

Fig. 12 Space-time diagram of the pressure signal in the leading edge of the impeller at φ = 0.0405

and has not yet created a new form of perturbation at the observed time scale.

Figure 12 shows the spatiotemporal expansion of the pressure signal at the impeller leading edge at φ = 0.0405 as the flow rate of the pressurizer continues to decrease. At this stage, the pressure wave propagates faster than the rotation speed of the impeller, with a disturbance frequency higher than the rotational frequency of the impeller but lower than the BPF. This indicates that the leading edge of the impeller is becoming unstable, with the pressure wave propagating along the circumferential direction.

The centrifugal pressurizer enters the destabilized condition at φ = 0.0390, as illustrated in Fig. 13. However, the pressure signal at the leading edge of the impeller indicates severe rotational instability in the centrifugal impeller. For the first two flow coefficients, the alternating high- and low-pressure regions continue to exhibit a frequency equal to the BPF of 5447.25 Hz. No low-frequency perturbations are observed in the leading edge of the impeller. However, the attenuation of the high- and low-pressure regions in the leading edge of the impeller induces a strong rotating pressure wave disturbance with a frequency of 1815.75 Hz—corresponding to 33.33% BPF. As indicated by the horizontal coordinate, rotational instability and rotational perturbations are initiated at 0–6 rpm. The rotational instability becomes fully developed by 6–8 rpm, with the pressure-signal waveforms at various circumferential positions completely formed at 8 rpm. At this point, the spatiotemporal diagram reveals the propagation path of the rotating pressure wave at the impeller leading edge, which exhibits a speed 40% higher than the rotational speed of the impeller.

(2) Amplitude–frequency characterization of centrifugal impeller pressure signals

Fourier transform was applied to the pressure signals under various operating conditions. The time-domain signals were converted into the frequency domain, enabling a clearer understanding of the signal strength. It also helps in identifying the onset of rotational instability in the centrifugal impeller. Figure 14 shows the pressure–frequency characteristics at the impeller leading edge for φ = 0.0412, φ = 0.0405, and φ = 0.0390. The z-, y-, and the x-axes represent the amplitude of pressure, circumferential angle, and the dimensionless frequency, respectively. The dimensionless frequency was obtained by dividing the local frequency by BPF.

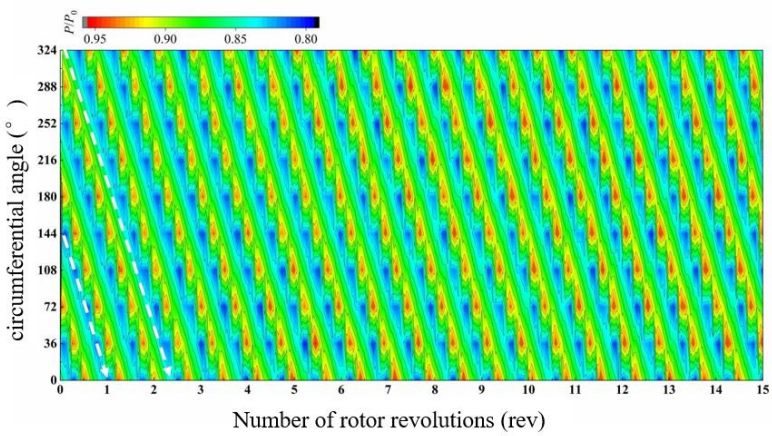

Fig. 13 Space-time diagram of the pressure signal in the leading edge of the impeller at φ = 0.0390

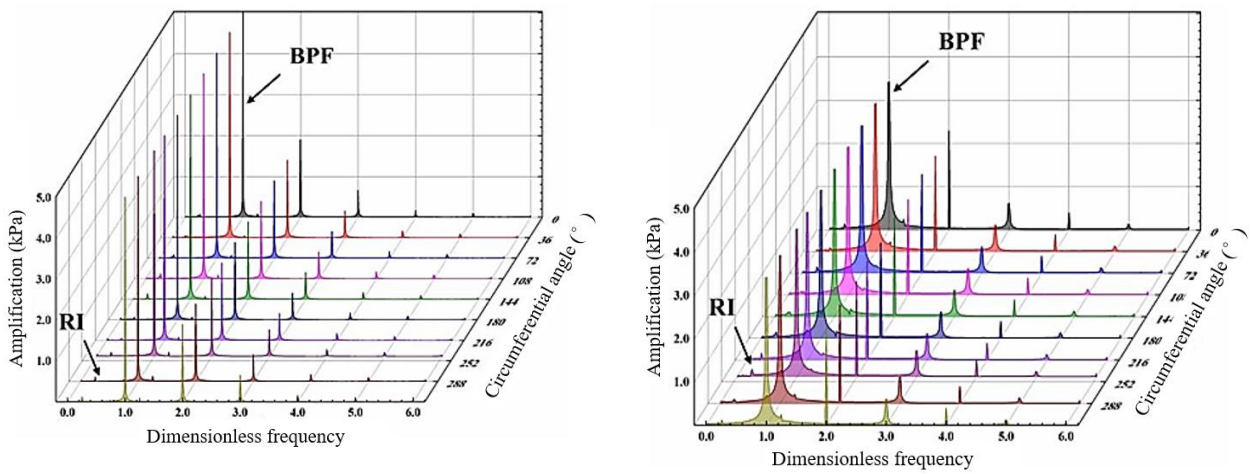

(a) φ = 0.0412 (b) φ = 0.0405

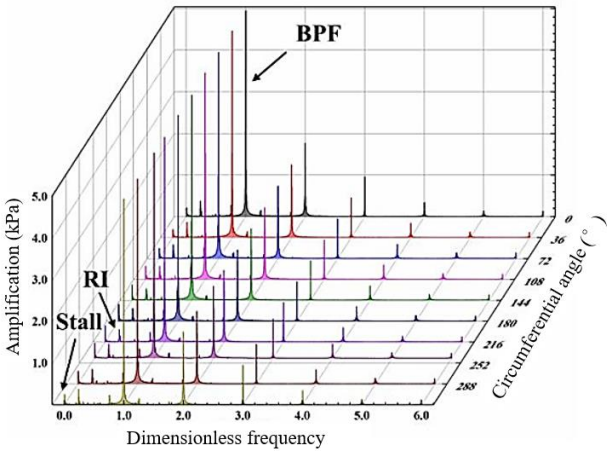

(c) φ = 0.0390

Fig. 14 Pressure amplitude–frequency characteristics of impeller leading edge

As shown in Fig. 14(a), pressure exhibits a more uniform spectral distribution along the circumferential direction of the impeller leading edge, suggesting steady flow and a uniform distribution of spatial parameters at this location in the impeller leading edge. Generally, a frequency corresponding to 30% of the peak BPF is indicative of rotational disturbance, and the observed frequency is consistent with this characteristics. The main frequency component of BPF exhibits an amplitude of 5.02 kPa. Additionally, a broad low-frequency band with smaller amplitudes is observed, with a frequency of 22.08%–25.24% of BPF. As shown in in Fig. 14(b), the spectral distribution of each pressure point along the circumferential position maintains good uniformity as the

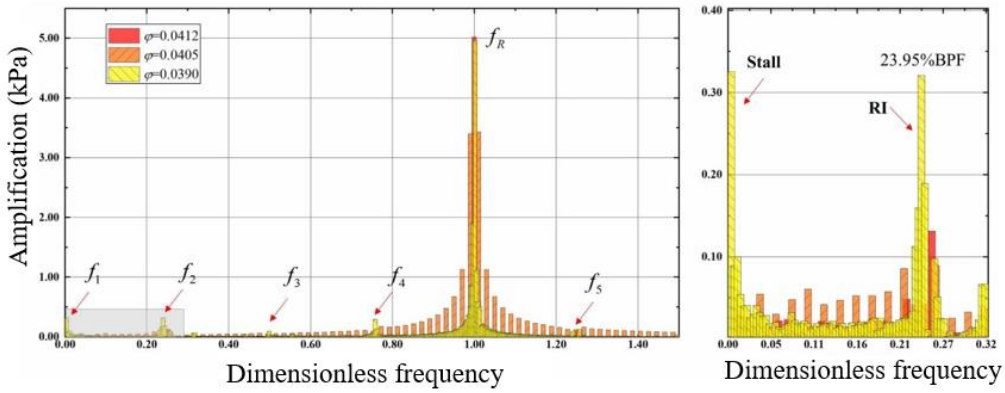

Fig. 15 Pressure amplitude–frequency characteristics at circumferential angle of 108° at impeller leading edge

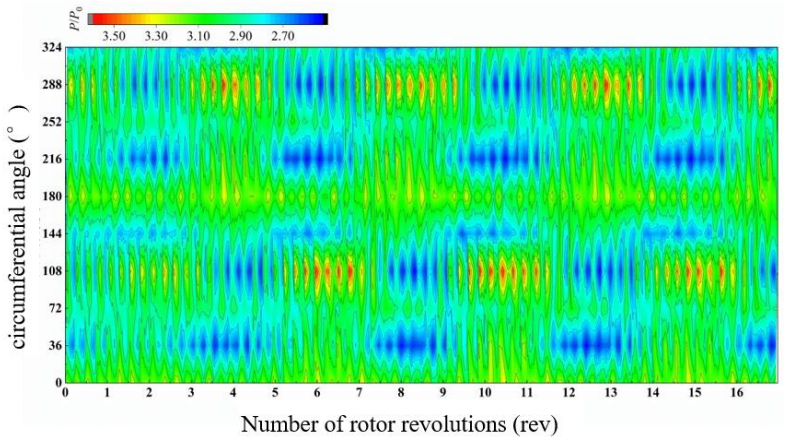

Fig. 16 Space-time diagram of the pressure signal at the inlet of the diffuser when φ = 0.0390

flow rate decreases. The amplitude of the main frequency components of BPF decreases to 3.41 kPa. However, the amplitude of the main frequency components of the adjacent frequency band increases, with a rotational perturbation frequency of 23.76%–25.74% of BPF. At φ = 0.0405, non-stationary flow begins to emerge; the disturbance at the impeller leading edge progressively intensifies and shifts toward low frequencies. While the amplitudes of the bands surrounding the main frequency components rapidly decline and shift toward low-frequency bands, the main amplitude of the frequency components gradually recovers to 4.95 kPa. At φ = 0.0390, the centrifugal impeller exhibits a progressive rise in the amplitude of rotational disturbance, which is uniformly distributed in the circumferential direction. This suggests that rotational instability was fully developed by this time.

Figure 15 displays the amplitude–frequency characteristics of the pressure signal at an angle of 108° in the circumferential direction. The pressure exhibits a significant degree of variations at this position. The bar chart illustrates the evolution of the amplitude–frequency characteristics in the impeller as the centrifugal compressor gradually approaches instability. Notably, as the flow coefficient further decreases to 0.0390, the frequency band in the major frequency region steadily narrows. However, when the flow coefficient drops from 0.0412 to 0.0405, the perturbations near the main frequency band is intensified. This indicates that, in the event of an impending instability in the centrifugal compressor, disturbances near the BPF initially increase while the compressor remains stable. As the flow rate continues to decrease, these disturbances subsequently diminishes and shift toward the low-frequency region. At φ = 0.0390, the five primary low-frequency components in the frequency distribution of the impeller leading edge exhibit a linear relationship with the BPF, where one component corresponds to the BPF and another to 23.95% of the BPF.

3.4 Spreader Rotational Stall Analysis

(1) Spatiotemporal characterization of diffuser pressure signals

As shown in Fig. 16, the pressure of the incoming flow in the diffuser of the centrifugal pressurizer at φ = 0.0390 is geographically and temporally dispersed. Four low-pressure bands can be observed in the diffuser leading edge at revolutions 0–3, with no significant high-pressure bands. At the third revolution, a high-pressure zone with a high core value first appears at an angle of 288° in the circumferential direction. Large-scale, low-frequency pressure oscillations are observed in this zone as it gradually expands and becomes stronger. The high-pressure zone begins to form at the fifth rotation, establishing a cyclic pattern at the periphery of 108°, with a consistent oscillation frequency.

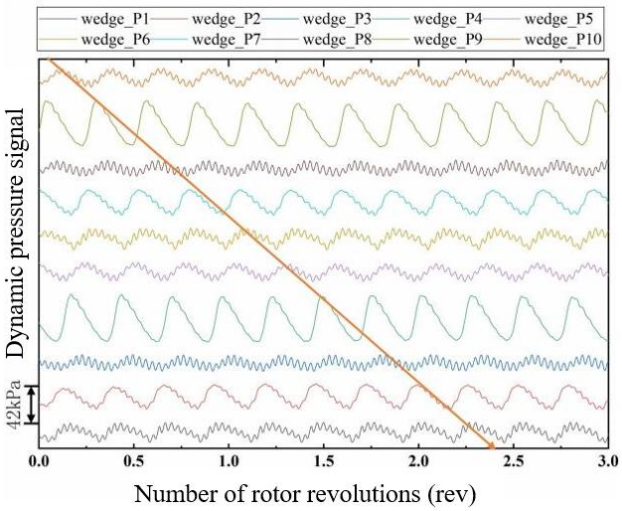

(a) **φ** = 0.0412

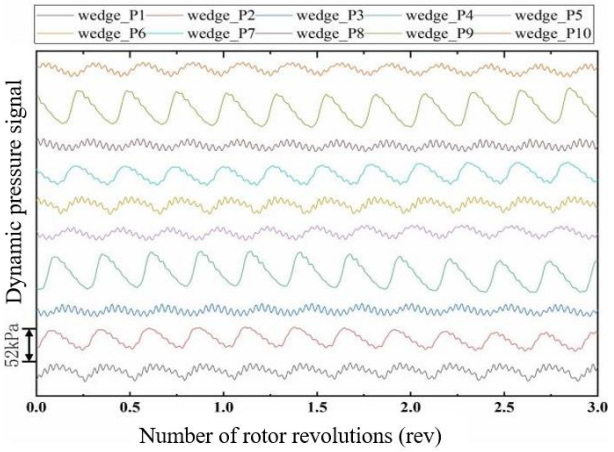

(b) **φ** = 0.0405

Fig. 17 Time-domain dynamic pressure

(2) Amplitude–frequency characterization of diffuser pressure signals

Figure 17 displays the dynamic pressure curves at the diffuser inlet for flow coefficients of φ = 0.0412 and 0.0405. At higher flow coefficients, the pressure fluctuations propagating along the circumferential direction at 40% of the rotational speed can be observed. This suggests that the unsteady flow structure becomes apparent earlier at the diffuser inlet than in the centrifugal impeller. The pressure signal at the diffuser inlet exhibits large-scale and low-frequency oscillations at φ = 0.0390, as illustrated in Fig. 17. At this point, the pressure signal is influenced by a few non-stereotypical effects, which should be examined further by analyzing the amplitude and frequency characteristics of the pressure signal using Fourier transform.

Figure 18 shows the amplitude–frequency characteristics of pressure at the diffuser inlet. (a) The pressure exhibits a large amplitude and a dominant frequency of 26.65% BPF. This suggests that the rotational perturbation initiated at the impeller leading edge intensifies as the flow moves downstream in the

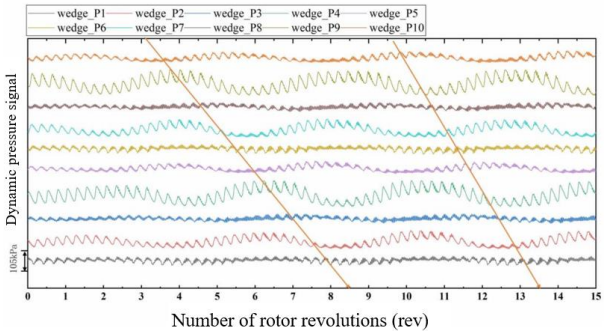

Fig. 18 Time-domain dynamic pressure at the inlet of diffuser when φ = 0.0390

channel and becomes a dominant perturbation at the diffuser inlet. The main frequency of 25.74% BPF (Fig. 19(b)) is consistent with the rotational disturbance of the impeller leading edge. However, in low-frequency regions, it transitions from a spike to a hump band, indicating that the stall characteristic frequency appears at the diffuser inlet at this time. As shown in Fig. 19(c), the stall frequency becomes the dominant frequency at the diffuser inlet, indicating that the diffuser has reached a stall condition. The increasing magnitude of the stall frequency at the circumferential positions of 36°, 108°, 216°, and 288° implies that the stall phenomena expands along the circumferential direction.

Fig. 20 shows the changes in the amplitude–frequency characteristics at the diffuser inlet. Multiple low-frequency bands at the diffuser inlet represent the doping and superposition of multiple nonconstant flows. At φ = 0.0412 and 0.0405, numerous perturbations are observed in the band regions lower than 25.52% BPF and 25.52%–49.86% BPF. At φ = 0.0390, the low-frequency bands shift leftward, and perturbations accumulate toward the lower frequencies, causing the diffuser to enter a complete stall state with a low frequency peak centered at 1.57% BPF and 23.55% IPF.

(3) Study on the mechanism of rotating stall back propagation in diffuser

Figure 21 depicts the distribution of instantaneous Mach number for the diffuser during the 95% lobe-height instability. The diffuser leading edge initially maintains a high degree of circumferential uniformity. Subsequently, a portion of the channel suction surface in the impeller begins to separate, resulting in a drop in circumferential uniformity as the flow declines. The initial excitation wave is produced at an angle of 45° to the blade's leading edge at the second revolution, which starts to move in the opposite direction of the impeller rotation. Five fully developed surge zones start to spread in the direction opposite to that of the impeller rotation at 3–7 rotations. Between the 7th and 15th revolutions, five shock wave regions and five low-speed stall clusters emerge, following a stable propagation path along the circumferential direction of diffuser blade channels. The propagation speed was 4.17% of the impeller rotational speed, with the propagation direction being opposite to that of the impeller rotation.

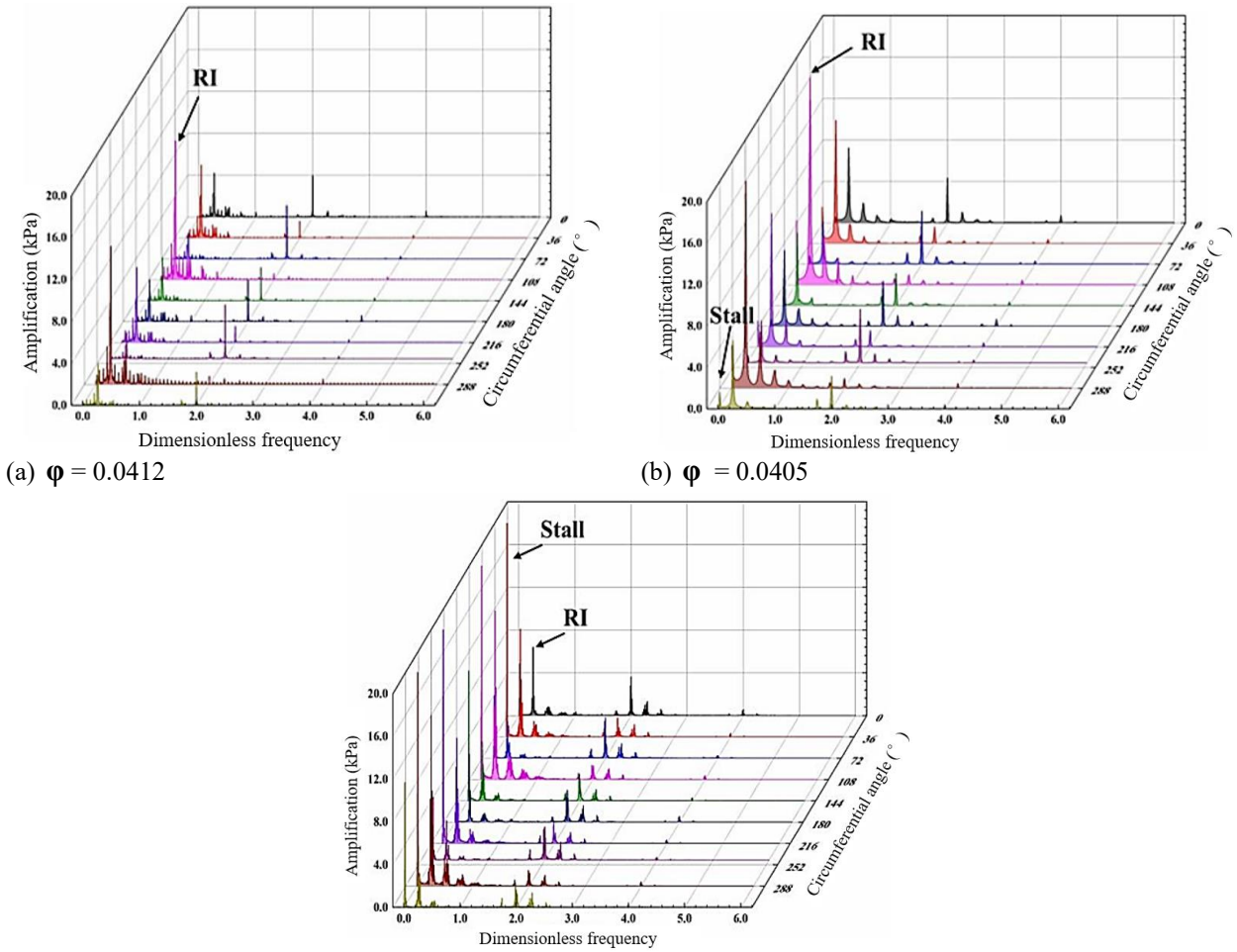

(a) φ = 0.0412 (b) φ = 0.0405

(c) φ = 0.0390

Fig. 19 Amplitude–frequency characteristics of pressure at the diffuser inlet

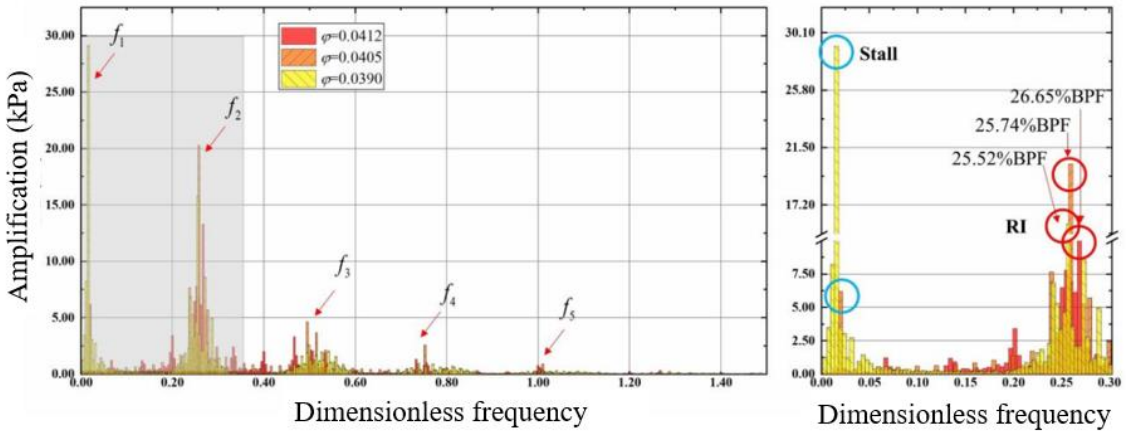

Fig. 20 Amplitude–frequency characteristics of Pressure at a circumferential angle of 108° in diffuser inlet

Additional insights were obtained on the mechanism of stall-cluster backpropagation in diffuser channels. At 1/4 turn, fragmented excitations appear at the leading edges of channels 1, 2, 6, and 7, as depicted in Fig. 22. When the excitation wave reaches its maximum intensity at channel 6, the suction side separates due to boundary layer interference, which decreases the angle of attack in channel 5 while increasing it in channel 7. Further separation due to excitation-induced boundary-layer interference is initiated at the 4/4 turn. The interplay between the excited wave, boundary-layer interference, and stall cluster triggers the reverse propagation of the stall cluster in channel 7. After one rotation cycle, an excitation wave is formed in channel 5. Two rotation cycles later, the flow in channels 6, 7, 4, and 5, along with the excitation wave, propagate in the direction opposite to that of impeller rotation.

4. CONCLUSION

This study employed numerical simulation techniques in both steady-state and unsteady-state conditions. We analyzed the differences between the flow

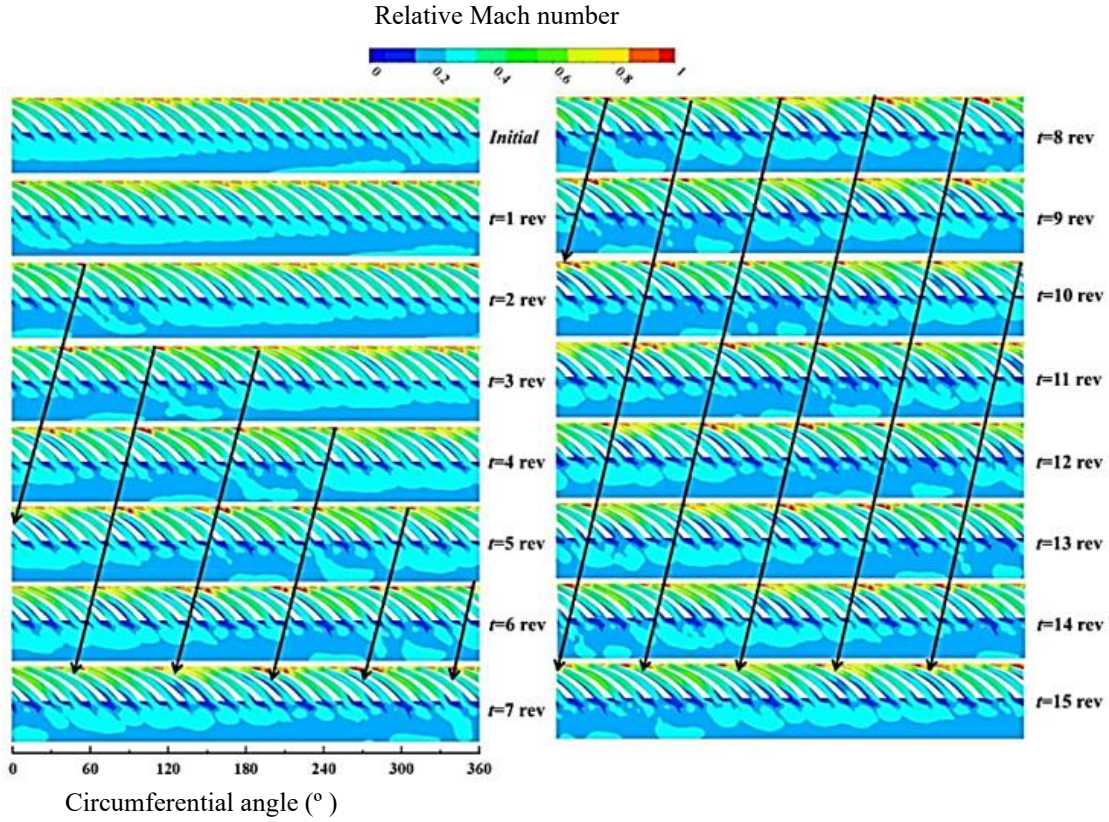

Fig. 21 Instantaneous Mach number at 95% blade span

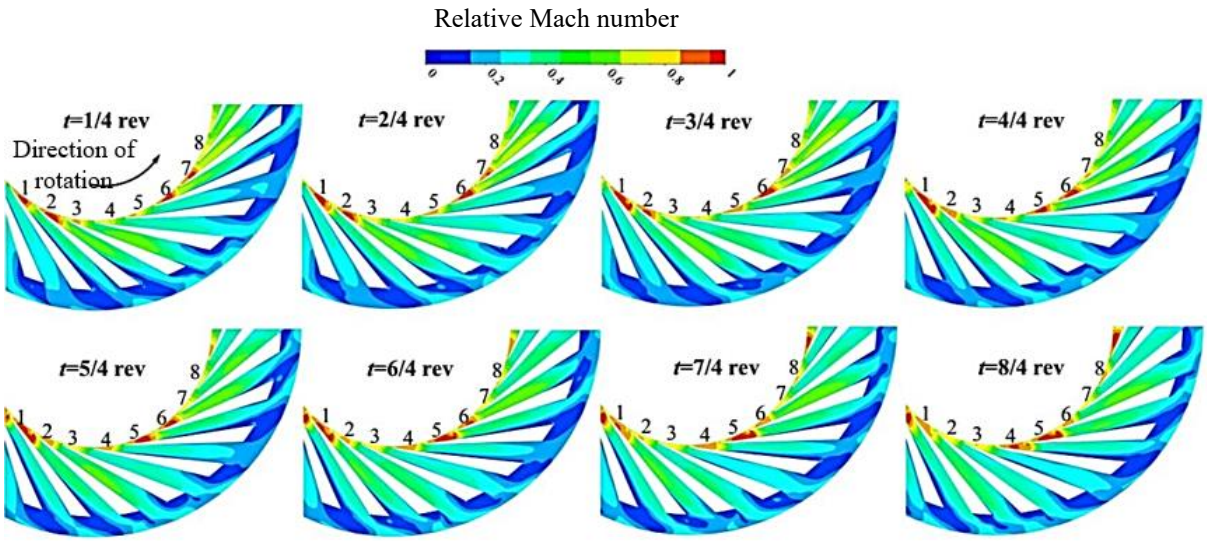

Fig. 22 Instantaneous Mach number for the backward-travelling stall

field of the single-channel model at constant flow and the flow field of the full-perimeter physical model. As the flow rate decreases, circumferential non-uniformity of the flow parameters progressively increased. Specifically, the maximum non-uniformity of the Mach number increased from 15.18% to 24.12% at the design point flow. In the full-perimeter model, the circumferential non-uniformity of the Mach number increased from 8.13% at the impeller leading edge to 25.52% at the diffuser leading edge at the blockage point. By contrast, at the blockage point, the maximum circumferential inhomogeneity of pressure increased from 4.96% to 7.05%, whereas at the design point, it increased from 8.90% to 13.73%.

The throttle valve model was employed to conduct unsteady-state simulation calculations for the full circumferential model of the centrifugal compressor. Signal analysis techniques, including spatiotemporal mapping, evaluation of amplitude–frequency characteristics, and low-pass filtering for signal discrimination, were used to investigate the pressure signals at key positions within the centrifugal compressor. The results indicated that the centrifugal compressor exhibits rotational instability as it becomes unstable. This rotation-induced pressure variations propagate in the circumferential direction at a speed of 40% of the impeller rotational speed, with a rotational perturbation frequency

of 1304.61 Hz and 23.95% of the BPF at the centrifugal impeller. Additionally, a stall characteristic frequency of 87.17 Hz was observed at the diffuser site. Flow field analysis further elucidated the process of stall mass dispersion in the opposite direction around the circle at a speed of 4.17% of the rotational speed of the impeller.

ACKNOWLEDGEMENTS

The authors would like to acknowledge the financial assistance from the State Key Laboratory of Clean and Efficient Turbomachinery Power Equipment (NO. EE280519)

CONFLICT OF INTEREST

All authors declare that they have no relevant relationships or competing interests that could have appeared to influence the work reported in this paper.

AUTHORS CONTRIBUTION

Yan Ping: conceptualization, methodology, and formal analysis. **Meng Wang**: analysis, manuscript revision, validation, and visualization. **Xiaodan Zhang**: editing the original draft. **Kunlun Bai**: formal analysis. **Feng Qu**: conducting the research. **Zhijian Tao**: research guidance. **Chenliang Wang**: writing, review, and editing.

REFERENCES

Day, I. J. (1993). Stall inception in axial flow compressors. *Journal of Turbomachinery, 115*(1), 1–9. https://doi.org/10.1115/1.2929209

Day, I. J. (2016). Stall, surge, and 75 years of research. *Journal of Turbomachinery*, *138*(1), 011001. https://doi.org/10.1115/1.4031473

Emmons, H. W., Pearson, C. E., & Grant, H. P. (1955). Compressor surge and stall propagation. *Transactions of the American Society of Mechanical Engineers*, *77*(4), 455-467. https://doi.org/10.1115/1.4014389

Fujisawa, N., Hara, S., Ohta, Y., & Goto, T. (2014, August). *Unsteady behavior of leading-edge vortex and diffuser stall inception in a centrifugal compressor with vaned diffuser.* Fluids Engineering Division Summer Meeting (Vol. 46223, p. V01BT10A015). American Society of Mechanical Engineers. https://doi.org/10.1115/FEDSM2014-21242

Ge, H., Chengwu, Y., Shixun, W., Shengfeng, Z., & Xingen, L. (2023). The investigation of mechanisms on pipe diffuser leading edge vortex generation and development in centrifugal compressor. *Applied Thermal Engineering, 219,* Part B(1), 119606. https://doi.org/10.1016/j.applthermaleng.2022.119606.

Greitzer, E. M., & Moore, F. K. (1986). A theory of post-stall transients in axial compression systems: part II—application. https://doi.org/10.1115/1.3239893

Han, G., Lu, X., Zhao, S., Yang, C., & Zhu, J. (2014). Parametric studies of pipe diffuser on performance of a highly loaded centrifugal compressor. *ASME. Journal of Engineering for Gas Turbines and Power, 136*(12), 122604. https://doi.org/10.1115/1.4027867

Hu, C. X., Geng, K. H., Zhang, C., & Yang, C. (2021). Study on the impact of blade installation angle on the aerodynamic performance and stall mechanism of centrifugal compressor diffusers. *Thermal Energy and Power Engineering. 36*(10), 77-84. https://doi.org/10.16146/j.cnki.rndlgc.2021.10.011

Marconcini, M., Bianchini, A., Checcucci, M., Ferrara, G., Arnone, A., Ferrari, L., & Rubino, D. T. (2016, June). *A 3D time-accurate CFD simulation of the flow field inside a vaneless diffuser during rotating stall conditions.* Turbo Expo: Power for Land, Sea, and Air (Vol. 49729, p. V02DT42A029). American Society of Mechanical Engineers. https://doi.org/10.1115/GT2016-57604

McDougall, N. M., Cumpsty, N. A., & Hynes, T. P. (1990). Stall inception in axial compressors. https://doi.org/10.1115/1.2927406

McKain, T. F., & Holbrook, G. J. (1997). *Coordinates for a high performance 4: 1 pressure ratio centrifugal compressor* (No. E-10833). https://ntrs.nasa.gov/api/citations/19970024917/downloads/19970024917

Sheng-ling, W. A. N. G., & Zheng-xian, L. I. U. (2019). Investigation of unsteady characteristics of rotating stall on eckardt centrifugal impeller. *Journal of Propulsion Technology, 40*(3), 542. http://jpt.tjjsjpt.com/EN/

Skoch, G. J., Prahst, P. S., Wemet, M. P., Wood, J. R., Strazisar, A. J., & Bamba, T. (1997). Laser anemometer measurements of the flow field in a 4:1 pressure ratio centrifugal impeller. *Journal of Turbomachinery, 119*(3), 412-421. https://doi.org/10.1115/97-GT-342

Spakovszky, Z. S. (2004). Backward traveling rotating stall waves in centrifugal compressors. *Journal of Turbomachinery, 126*(1), 1-12. https://doi.org/10.1115/1.1643382

Sun, Z., Zheng, X., & Kawakubo, T. (2018). Experimental investigation of instability inducement and mechanism of centrifugal compressors with vaned diffuser. *Applied Thermal Engineering, 133*, 464–471. https://doi.org/10.1016/j.applthermaleng.2018.01.071

Wang, M. (2020). *Numerical research on the flow field in axial compressor under unstable working conditions by using the harmonic balance method*, Harbin Engineering University. https://link.cnki.net/doi/10.27060/d.cnki.ghbcu.2020.001738

Xu, L., Liu, Z., Li, X., Zhao, M., Zhao, Y., & Zhou, T. (2023). Dynamic mode characteristics of flow

instabilities in a centrifugal compressor impeller. *Aerospace Science and Technology, 142*, 108707. https://doi.org/10.1016/j.ast.2023.108707

Xue, X., & Wang, T. (2020). Experimental study on inducement and development of flow instabilities in a centrifugal compressor with different diffuser types. *Journal of Thermal Science, 29*, 435-444. https://doi.org/10.1007/s11630-020-1223-4

Yoon, Y. S., & Song, S. J. (2014). Analysis and measurement of the impact of diffuser width on rotating stall in centrifugal compressors. *Journal of mechanical science and technology, 28*, 895-905. https://doi.org/10.1007/s12206-013-1157-9

Zhang, H., Yang, C., Wang, W., Yang, C., & Li, Y. (2022). Experimental investigation of the pre-stall and stall evolution in a centrifugal compressor with a volute. *Journal of Turbomachinery*, *144*(8), 081012. https://doi.org/10.1115/1.4053838

Zhang, L. (2020). *Study on Two Stall Modes in Centrifugal Compressor Wide Vaneless Diffuser* [D]. North China Electric Power University, https://link.cnki.net/doi/10.27139/d.cnki.ghbdu.2020.000659

Zhang, L., Zheng, Z., Zhang, Q., Zhang, L., & Li, K. (2020). Study of rotating stall in a centrifugal compressor with wide vaneless diffuser. *Journal of Thermal Science*, *29*, 743-752. https://doi.org/10.1007/s11630-020-1214-5

Zhang, Q. (2021). Induced Mechanism and Energy Loss of Rotating Stall in the Centrifugal Compressor with Vaneless Diffuser [D]. North China Electric Power University (Beijing). https://link.cnki.net/doi/10.27140/d.cnki.ghbbu.2021.000014

Zhang, Q., Chen, R., Zhang, L. & Zhang, L. (2021). Numerical investigation of rotating stall in centrifugal compressor with wide vaneless diffuser. *Turbine Technology, 63*(1), 1–4+64. https://link.cnki.net/doi/CNKI:SUN:QLJV.0.2021-01-001

Zhang, Y. J., Han. G., Li, Q. K., Zhang, Z. Q., Zhang. Y. F. & Lu, X. G. (2022). Stall Mechanism in an Ultra-High-Pressure-ratio Centrifugal Compressor. *Journal of Engineering Thermophysics, 43*(02), 309-315. https://link.cnki.net/doi/CNKI:SUN:GCRB.0.2022-02-006

Zheng, Z. (2019). Research on the Mechanism and Criteria for Discrimination of Rotating Stall in Wide and Narrow Vaneless Diffusers of Centrifugal Compressors. North China Electric Power University. https://kns.cnki.net/kcms2/article/abstract?v=ZH6vWTMDPUJem8XhNT13_Y2GSnx0XfvLi5c9n_fZN82NeXXb_o944i4Sc41B4Ou4qXkEYA5hmcBTP_97tcZ_BQgLpxLczjTT306SAbZ2qlW004dU1ND5tSwOPZj_hh47G1nNf5v2Fq8VeAQOFaSBIRsHMaLTC7FBxc83uy7jRgMyJWBp8l2sMyZSexVsKG4k&uniplatform=NZKPT&language=CHS